Precise DEM extraction from oblique imagery of Svalbard in 1936

Luc Girod[1], Niels Ivar Nielsen[1], Frédérique Couderette[1,2], Christopher Nuth[1], and Andreas Kääb[1]

[1]Department of Geosciences, University of Oslo, Postboks 1047 Blindern, 0316 Oslo, Norway
[2]École Nationale des Sciences Géographiques, 6 et 8 Avenue Blaise Pascal, Cité Descartes, 77420 Champs-sur-Marne, France

Correspondence to: luc.girod@geo.uio.no

Abstract. Stretching time series further in the past with the best possible accuracy is essential to the understanding of climate change impacts and geomorphological processes evolving on decadal-scale time spans. In the first half of the twentieth century, large part of the polar regions was still un-mapped or only superficially so. To create cartographic data, a number of historic photogrammetric campaigns were conducted using oblique imagery, easier to work with in un-mapped environments as collocating images is an easier task for the human eye given a more familiar viewing angle and a larger field of view. Even if the data obtained from such campaigns gave a good baseline for the cartography of the area, the precision and accuracy of it is to be considered with caution. Exploiting the possibilities arising from modern image processing tools and re-processing the archives to obtain better data is therefore a task worth the effort. The oblique angle of view of the data is offering a challenge to classical photogrammetric tools, but the use of modern Structure-from-Motion (SfM) photogrammetry offers an efficient and quantitative way to process this data into terrain models. In this paper, we propose a good practice method for processing historical oblique imagery using open source free software and illustrate the process using images of the Svalbard archipelago acquired in 1936 by the Norwegian Polar Institute. We create 5m-resolution DEMs and orthoimages and compare them to modern data.

1 Introduction

The processing, or re-processing, of historical imagery into Digital Elevation Models (DEMs) and orthoimages enables extending time series for long-term geomorphological change analysis (Csatho, 2015; Mölg and Bolch, 2017). One of the main source of such data is archived aerial imagery from historical photogrammetric surveys (Kääb, 2002; Vargo et al., 2017). However, compared to the processing of modern digital imagery, the task of processing scanned film imagery comes with added challenges:

- The scanning usually does not conserve a consistent internal geometry and the images need to be normalized.

- No metadata is present in the files. If not always strictly necessary, it is often very helpful to have access to (1) calibration information (i.e. calibrated focal and position of fiducial marks) and (2) location information in the form of ground control points (GCPs) or navigation data.

- Stereo-overlap is low (typically 60% along-track and 20% cross-track) compared to modern standards.

Processing nadir imagery over mostly stable land areas where good quality modern data is available for reference has proved easily accomplished and effective (Gomez et al., 2015). More challenging scenarios are however common, for instance, large data sets over Antarctica include regions with very little off-glacier stable areas to provide sufficient Ground Control Points (GCPs) (Child et al., 2017).

Another common type of imagery is oblique imagery. It was acquired primarily in areas previously un-mapped, or only superficially so. Such imagery it has the advantage of providing a point of view that is easier to apprehend for a human user, and where identifiable points can be seen from long distances (even if the image quality goes down with distance from the camera position). However, for computer-based processing, oblique data adds a layer of challenges compared to nadir imagery:

- The footprint of each image is not very well defined as it extends to infinity in a cone shape and excludes part of the ground because of terrain occlusion (e.g. behind ridges and peaks). Therefore, the term *viewshed* is employed here instead of footprint.

- The resolution of the imagery is dependent on (1) the distance to the camera (the further away to the camera, the lower the resolution) in a much bigger way than nadir imagery (here, the variation in the camera-to-ground distance can vary several folds!) and (2) the slope of the terrain (slopes facing the camera will have a very high amount of pixels per horizontal unit of surface).

In this paper, we present and discuss the challenges and solutions related to the processing of oblique (e.g. non-nadir) historical imagery using the 1936 survey of the Svalbard archipelago as an example. We then provide some concise comments on the observed change in elevation over glaciers and rock glaciers.

2 Data: 1936 images of Svalbard

In the summers of 1936 and 1938, Norwegian expeditions lead by Docent Adolf Hoel went to Svalbard to photograph the area from the air. Bernhard Luncke was in charge of the planning and acquisition of aerial photographs. Their goal was to collect images suitable for creating topographic maps of Svalbard in 1:50 000 scale and contour interval of 50m (Nuth et al., 2007). The Norwegian Navy provided the expedition with a M F 11 scout plane with crew. A Zeiss camera (film format 18×18 cm, focal length 210.71mm) was mounted in a stabilizing cradle at the side of the plane. The photographs were taken at an altitude of around 3000m along the coast and 3500m inland, with the optical axis of the camera pointed 20° below the horizon, or 70° off-nadir, making them high-oblique (Luncke, 1936). The overlap between two images is approximately 60%.

In 1936, good weather conditions allowed for a total effective flight time of 89 hours. 3300 images covering an area of 40 000km² or nearly $\frac{2}{3}$ of the total area of Svalbard were taken. The areas covered were Barentsøya, Edgeøya and most of western Spitsbergen. Fig. 1 shows where aerial photographs were taken during the 1936 expedition (Luncke, 1936).

The goal of the 1938 expedition was to photograph the areas that were not covered in 1936. Bad weather conditions and technical problems prevented the completion of the planned acquisition, but 48 hours of flight time resulted in 2178 photographs

covering a total area of about 25 000km^2. In total the two expeditions in 1936 and 1938 resulted in 5478 high-oblique aerial photographs that cover most of Svalbard.

The photographs are owned and managed by the Norwegian Polar Institute (NPI). In the 1990s, the institute hand digitized the maps made from the data, and in 2014, the original films were scanned with a photogrammetry-grade scanner at a 13.5

5 micron resolution, resulting in 14500x14500 pixel image files. The first attempt at processing the data into native DEM (not computed from map data) using a photogrammetric workstation was done for (Etzelmüller and Sollid, 1996) over the Erikbreen glacier. Other processing of subsets of the imagery were attempted by (Midgley and Tonkin, 2017), using 3 images over Midtre and Austre Lovénbreen, and (Mertes et al., 2017), using 25 images over Brøggerhalvøya.

In this paper, a subset of 72 pictures taken in the summer 1936 in two lines along the western (43 pictures) and eastern (29

10 pictures) coasts of the Prins Karls Forland, eastern Svalbard, were used as an example (see Fig. 1). The island is a thin band of land covered for the most part by a linear mountain range and some strandflats in the south (not covered by this study). Alpine and marine terminating glaciers, and rock-glaciers are present in most of the valley of the island. Some of the illustrative figures in this paper are taken from (Nielsen, 2017) who used images over Barentsøya (SE Svalbard). As ground truth and as a source of ground control points (GCPs, see Section 3.4), we used the NPI DEMs from 1990 and 2008, and the TANDEM-X IDEM

15 from 2010.

3 Methods

Historical oblique imagery can be processed through a nearly unmodified typical Structure-from-motion photogrammetric pipeline, described in this section, and in Fig. 2.

3.1 Scanning and geometric normalization

20 The scanning of images usually results in images that are not all the exact same dimension, and fiducial marks are not necessarily positioned exactly at the same place. To simplify the image assimilation into the photogrammetric process, they have to be geometrically normalized to be all in the same geometry so that the images' resolution and fiducial marks' positions are the same, and the internal calibration of all the images is the same. Calibration data on the real metric coordinates of the fiducial marks may be available, but an initial estimate should be sufficient for the normalization. In any case, calibration performed

25 on the camera at the time of acquisition would not be taking into account the aging process that the film experienced before having been scanned.

In order to compute the parameters of the 2D-transformation (translation, rotation and scaling) for each image, the fiducial marks need to be identified, either manually, or through an automated process. If fiducial marks are in the center inside of a clear target such as a cross, it is easy to find them automatically. However, this is not the case for our data, where the fiducial

30 mark is a single dot in the film (see Fig. 3). Using the shape of the frame, it is possible to approximate the position for this point, then it is possible to identify the brightest circular blob (i.e. the fiducial mark) and record its position (Nielsen, 2017). Once fiducial marks are recorded for an image, it can be re-sampled to the normalized geometry.
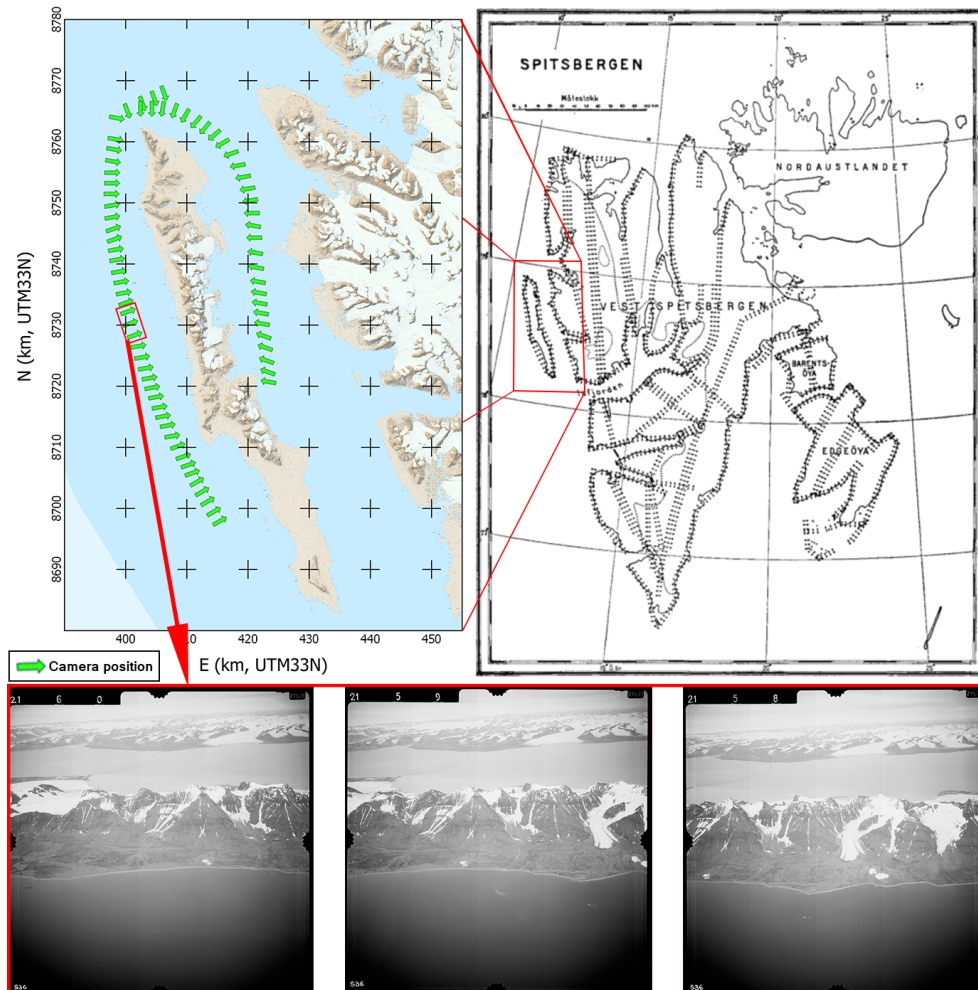
Figure 1. Left: Map of the example area with the positions of the camera and their pointing direction over Prins Karl Forland. Right: map of Svalbard with the position of the images taken in 1936, from (Luncke, 1936). Bottom, example of triplet of images over Prins Karl Forland.

3.2 Tie point extraction

To be able to run a structure-from-motion based bundle adjustment, tie points need to be extracted from the imagery. The SIFT algorithm (Lowe, 2004) proved efficient at finding such tie points between adjacent images on land areas, even in the background of the images, hence also providing tie points between not directly adjacent images. However, SIFT cannot provide tie points between two images if the pointing directions are too different (over $30°$), which complicates the automatic relative orientation of large group of images since images taken from two different flight lines usually do not satisfy this requirement. For instance, images from the two opposing lines of flight used in our test case over Prins Karl Forland have an angle between
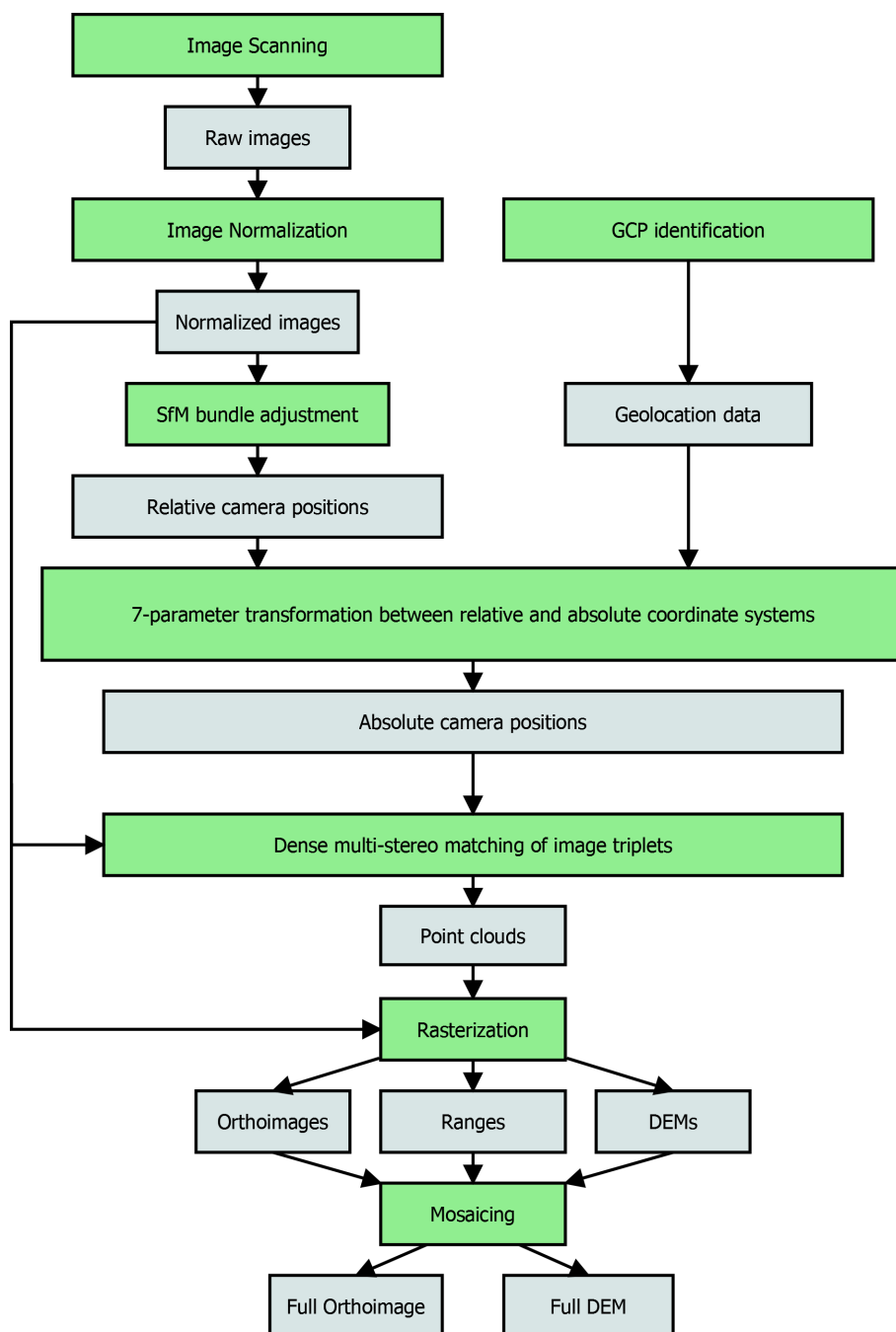
Figure 2. Workflow of the Structure-from-motion photogrammetric pipeline used in this paper. Data is represented in gray and processes in green.
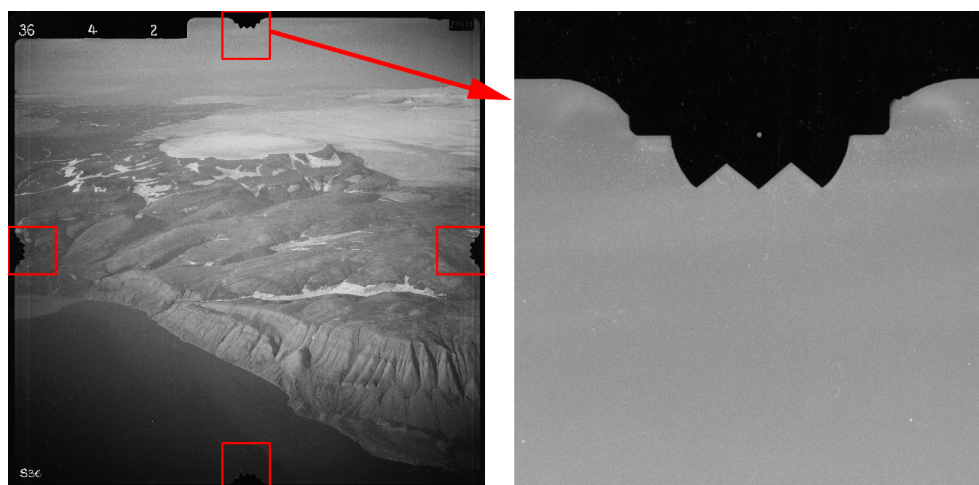
Figure 3. Fiducial mark in an image from 1936 over Svalbard and a close up on the top one.

the lines of sight of $\approx 140°$. Therefore, in many cases, each flight line needs to be processed individually until the final mosaicking step (see Section 3.7).

3.3 Relative orientation and calibration

Now that the images are in a coherent internal geometry, the camera can be calibrated and a bundle adjustment process can be performed. The NPI archives contained a single piece of information about the camera used for our data: its focal length of 210.71mm. From this information, we could initialize the calibration process. The calibration (in the form of a Brown distortion model (Brown, 1966, 1971)) is initialized on a small subset of 5 images that present a good amount of tie points, well distributed in the images and covering the most of the image field. The other images are then added to the block to obtain a relative orientation of the image set.

3.4 Absolute orientation

The absolute orientation requires ground control points (GCPs), but no such points were recorded at the time of acquisition in 1936. It is therefore necessary to rely on modern data coverage of the area to gather GCPs from. To do so, prominent points in stable areas are identified both in the historical images and in a modern source. This step is very challenging since most of the lowlands cannot be considered stable over 50 years: ice-cored moraines and permafrost areas, thermokarst processes, unstable cliffs, or simply erosion renders the lowlands unstable and generally unrecognizable reliably. Some areas are also challenging to recognize because of the vastly different ice cover over the terrain. Therefore only bedrock features can be used and it is easiest to identify the mountain tops as GCPs, but even these points are not always very accurate, as the reference DEMs can be of low resolution and often soften the mountain ridges and peaks in particular. The process is further complicated by the strong obliqueness of the historic imagery, making the task of recognizing even very prominent features difficult. The

automation of the process used by (Vargo et al., 2017), finding tie points between modern georeferenced images and historical images is here impossible to put in action as no modern images taken in a similar configuration are available. The possibility of mis-identification involves the requirement of more GCP candidates that can *a posteriori* be corrected or filtered out.

Once GCPs are identified, a rigid 7-parameters (3D translations and rotation, and scaling) transformation is computed first,
5   then the camera calibration is re-estimated using the GCPs.

3.5   Point-cloud generation

To generate point-clouds, images are grouped into triplets of subsequent images in a line of flight. There is no point using more than three images as the area imaged in the central image of a triplet (used a the master image) will not be seen on further images because of the $ca. 60\%$ overlap. Each triplet goes through for a dense correlation process (Furukawa and Ponce, 2010),
10   performed in image geometry: a 3D point in the ground coordinate system corresponding to each pixel in the master image is estimated.

In order to only compute data on areas of interest, the master images need to be masked, as trying to get data out of the entire viewshed area would make the process slower, add noise to the data and create heavier files that are harder to work with. Specifically, one should mask the sea, the sky, clouds, and background land visible in the image but not in the area of
15   interest. The masking can be completely manual, but it is then a very tenuous task, especially for large datasets. It is possible to automate the detection of sea, sky and clouds by running an entropy based texture analysis, but differentiating foreground and background is more difficult (Nielsen, 2017) (see Fig. 4). Additional masking through the use of a polygon defining the area of interest in ground coordinate is also possible, either by back-projecting a known DEM of it into the individual, then-known image geometries, or by filtering out-of-area points during the iterative dense correlation process.
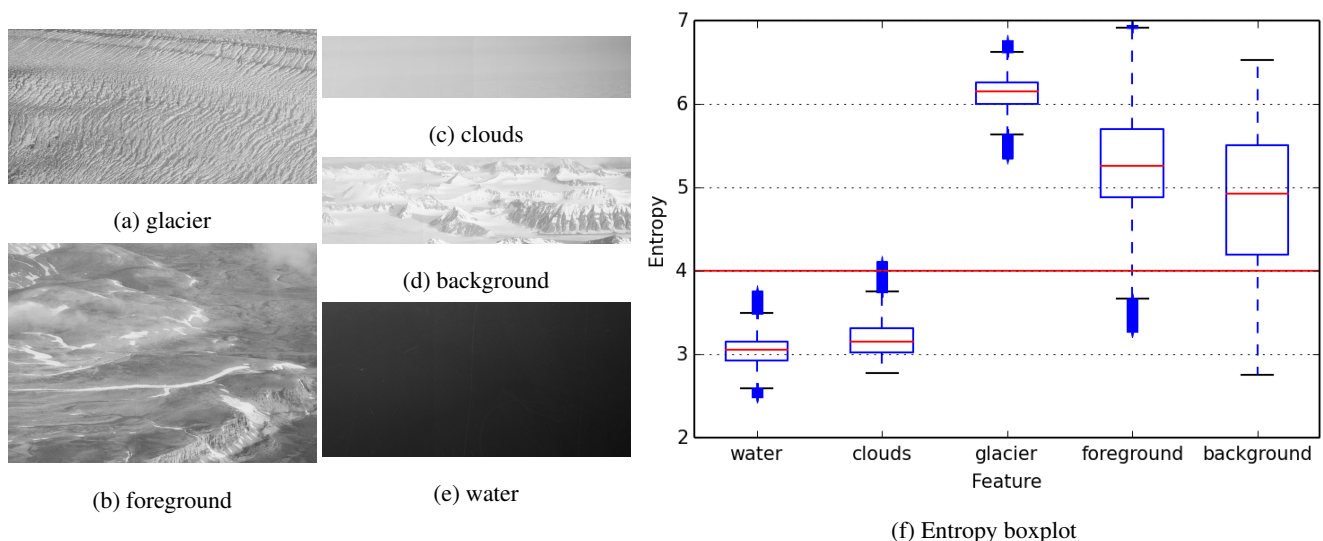
Figure 4. Entropy response values for samples of different terrain features.

3.6 DEM and orthoimage generation

Once a three-dimensional point cloud has been generated, it can be filtered to remove noise and then turned into a number of different raster (2D) files. The first step in the filtering is to simply remove points that are out of the area of interest (defined by a polygon in X and Y) and that have a Z component outside of the known minimum and maximum altitudes in the area (with a
5   small margin of error to compensate for imperfect georeference). Noise filtering is then performed to remove local outliers. A third pass, manual this time, is however still necessary in most cases, as some elements of the terrain such as mountain ridges or the sea shore can be the source of erroneous data in the form of rays of points in the approximate direction of the optical rays (see Fig. 5).
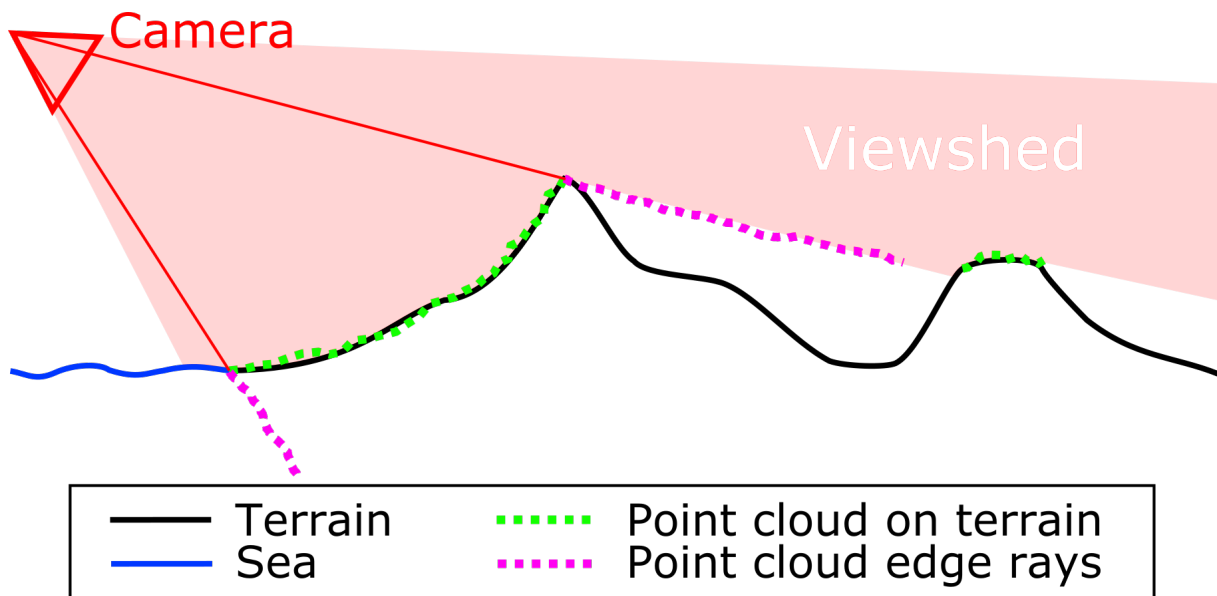
Figure 5. Representation of erroneous data points created by mountain ridges and sea shore in the approximate direction of the optical rays. Note that the terrain occluded by the foreground mountain, therefore not included in the viewshed, is not represented in the point cloud.

      The clean three-dimensional point cloud is then used as the input for raster data creation. The resolution and corner coordi-
10   nates of the raster needs to be determined first. From the 1936 Svalbard photos, a 5m GSD product can be reliably generated in the areas presented in this paper without requiring extensive void filling. Here, we want to create an orthoimage (a raster of colors, here gray scales, see Fig. 6A), a DEM (a raster of elevation, see Fig. 6B), and a record of the distance between the points and the camera (range, see Fig. 6C, to be used later in the mosaiking process, see Section 3.7, and as an indication for error propagation). here, each cell of the rasters is given the mean value of the points in a radius around the cell center.
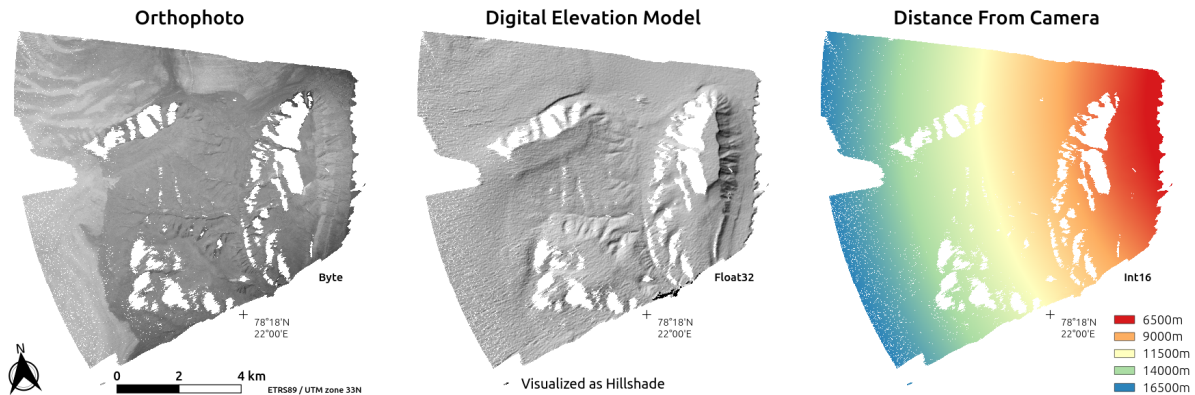
Figure 6. Rasters extracted from a single point cloud. A: Orthoimage. B: Hillshade of the DEM. C: Distance to the camera.

3.7 DEM and orthoimage mosaicking

Once all rasters are generated for each point cloud, they can be mosaicked using the distance raster as an input for a Voronoï process: for each point of the final raster, the color/elevation from the set of raster presenting the lowest range value (distance to camera) is selected and recorded, creating the data shown in Fig. 7.

5   This simple approach creates visible boundaries between each area, especially in the orthoimage, and some radiometric equalization could also be performed. The mosaicking could be avoided by first merging all the point clouds and performing the rastering process only once from the full combined cloud, using a weighting system based on the point to camera distance value. However, given that individual clouds can be composed of over fifty million points, the amount of memory required to load dozens of clouds in a software (either for merging or rastering) is an almost impossible task, even for a heavy workstation.

10 ## 4   Results

In this section, we discuss first the final product quality, then point out the weaknesses remaining in the data that required manual filtering.

4.1   Data quality

In order to determine its accuracy, our 1936 elevation data was compared to other DEMs. The NPI most modern DEM product 15 (S0 product) over the area is extracted from the 2008 aerial survey of Svalbard, and is also at 5 m GSD, while the NPI 1990 DEM is at 20 m GSD. The 2010 Tandem-X IDEM product at 12m GSD over the area is of acceptable quality, except for west facing steep slopes, where obvious outliers and data voids are present. This is due to the view angle of the radar satellite that was from the east (descending) during the acquisition. Comparison with either products on low-slope, relatively stable areas
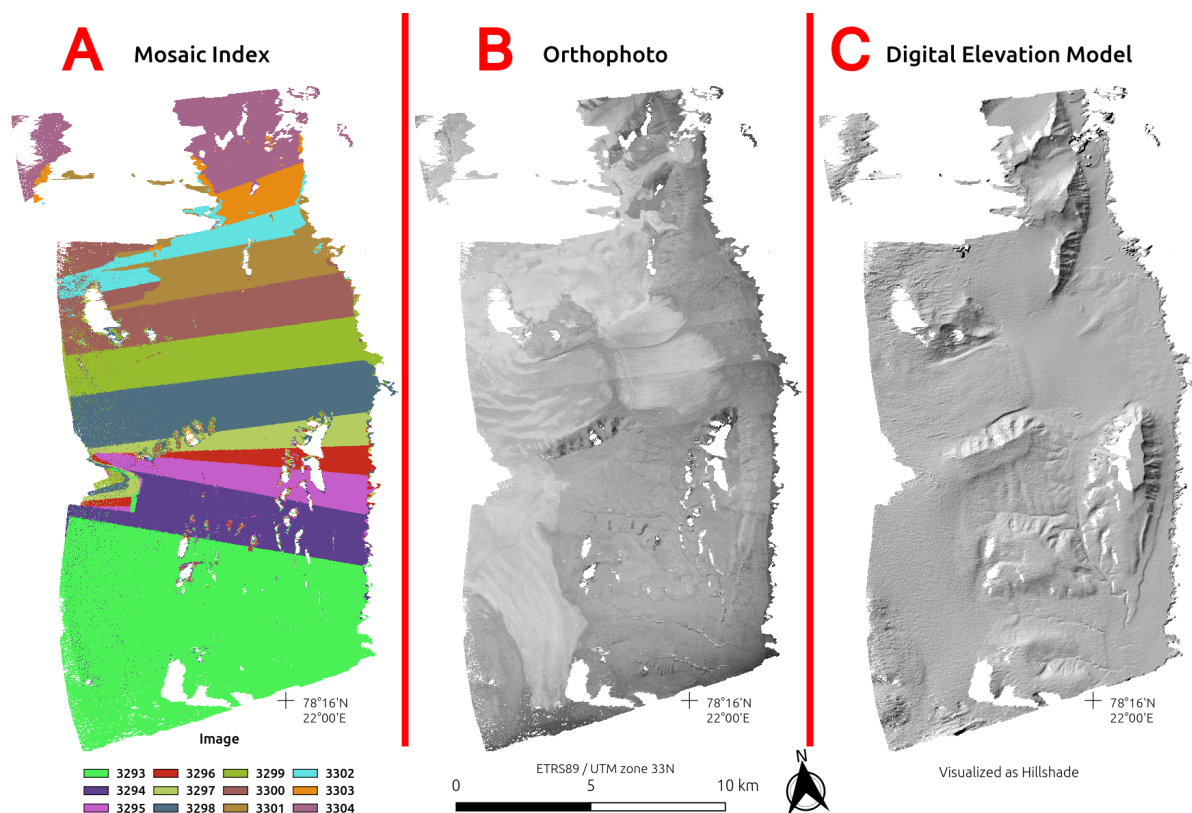
Figure 7. Rasters mosaic. A: Map of the mosaic, each color representing an individual source point raster. B: Mosaiked orthoimage. C: Mosaicked hillshade DEM.

that do not present obvious errors returns a standard deviation for the elevation errors of $2\,m$, while selecting a larger zones containing diverse terrain yielded a value of $5.4\,m$.

These values are significant improvements on the $12.2\,m$ reported by (Nuth et al., 2007) in the comparison of the digitized 1936 map DEM with the 1990 NPI DEM. It is also better than the $5.2\,m$ value reported by (Mertes et al., 2017), obtained by comparing the NPI 2010 DEM with the data obtained over Brøggerhalvøya, only over filtered stable ground. (Midgley and Tonkin, 2017) processed a subset of three images of the Brøggerhalvøya series used by (Mertes et al., 2017), hence representing a relatively small area, and reported similar values: $2.9\,m$ for the relatively flat pro-glacial area and $8.5\,m$ when mountain slopes were included in the analysis.

4.2 Selected geomorphological highlights

The key reason to process the 1936 photos using modern technology is that it can be used as a baseline to assess long term change related to glacial and periglacial processes, adding important early data points in the time series of DEMs over the area. By comparing this data with modern products, a nearly centennial glacier mass balance could be estimated, for instance. We
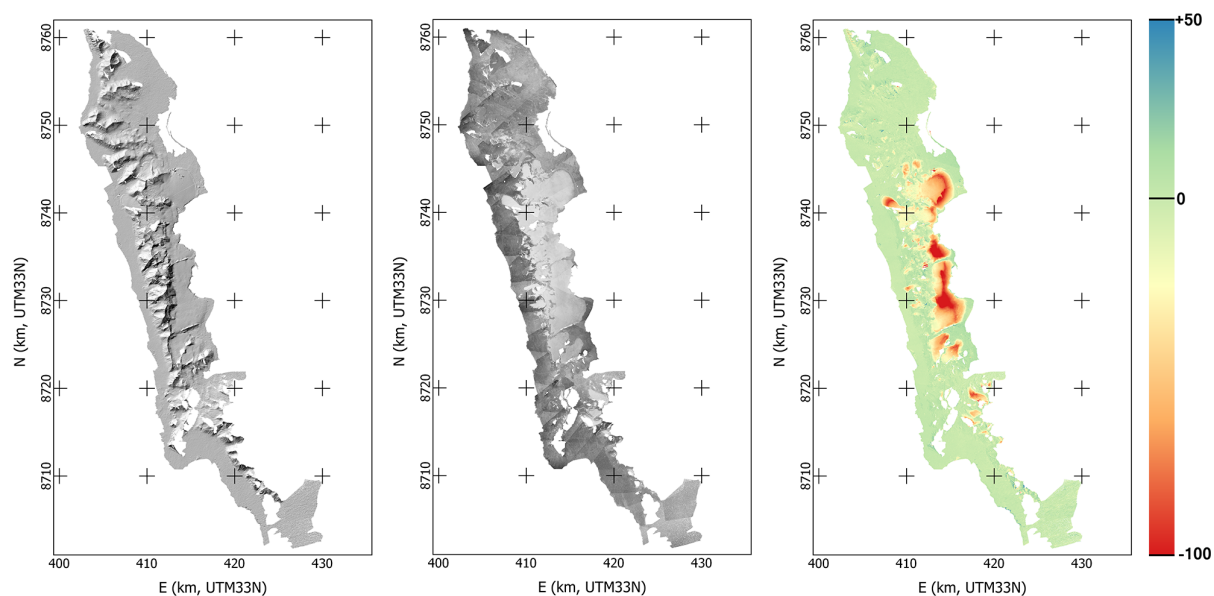
Figure 8. Overview of the data resulting from the processing of the 1936 images over Prins Karl Forlands. From left to right: Hillshade, orthoimage, DEM difference with the NPI 2008 DEM.

show here three examples of different processes observed in the differential DEM (dDEM) between our product based on the 1936 imagery and the most recent DEM from the NPI computed from imagery from 2008.

4.2.1 Alpine glacier example: Millerbreen

In this example, we show the data gathered for the alpine glacier Millerbreen. In 1936, it was land terminating, reaching nearly

5   to its moraine, while in 2008 (and up to today), a large part of the front calves into a lake that formed inside the barrier formed by the moraine. Fig. 9 shows the dDEM over the glacier as well as a profile-line over the two DEM and the dDEM. We can see that during the 72 years separating the two datasets, the glacier retreated by approximately $900\,m$ ($12.5\,m.year^{-1}$), losing up to $95\,m$ of ice thickness. The dH curve is very typical for a retreating glacier, linearly going from zero at the old tongue edge to a maximum loss at the new tongue edge, and then reaching back to zero at a slower rate up to the top edge of the accumulation

10   zone.

4.2.2 Marine terminating glacier example: Søre Buchananisen

Søre Buchananisen is a large marine terminating glacier that experienced a significant retreat (up to $2.0\,km$) in the 72 years separating the two data sets ($27.8\,m.year^{-1}$). The dDEM shows the new ice edge very clearly as the elevation loss is total in the retreated area and only partial from the edge of the ice cliff upwards. The change of the glacier seems to display several

15   basins, with the northern and southern parts retreating fast, separated by a (now) land terminating middle section. The southern
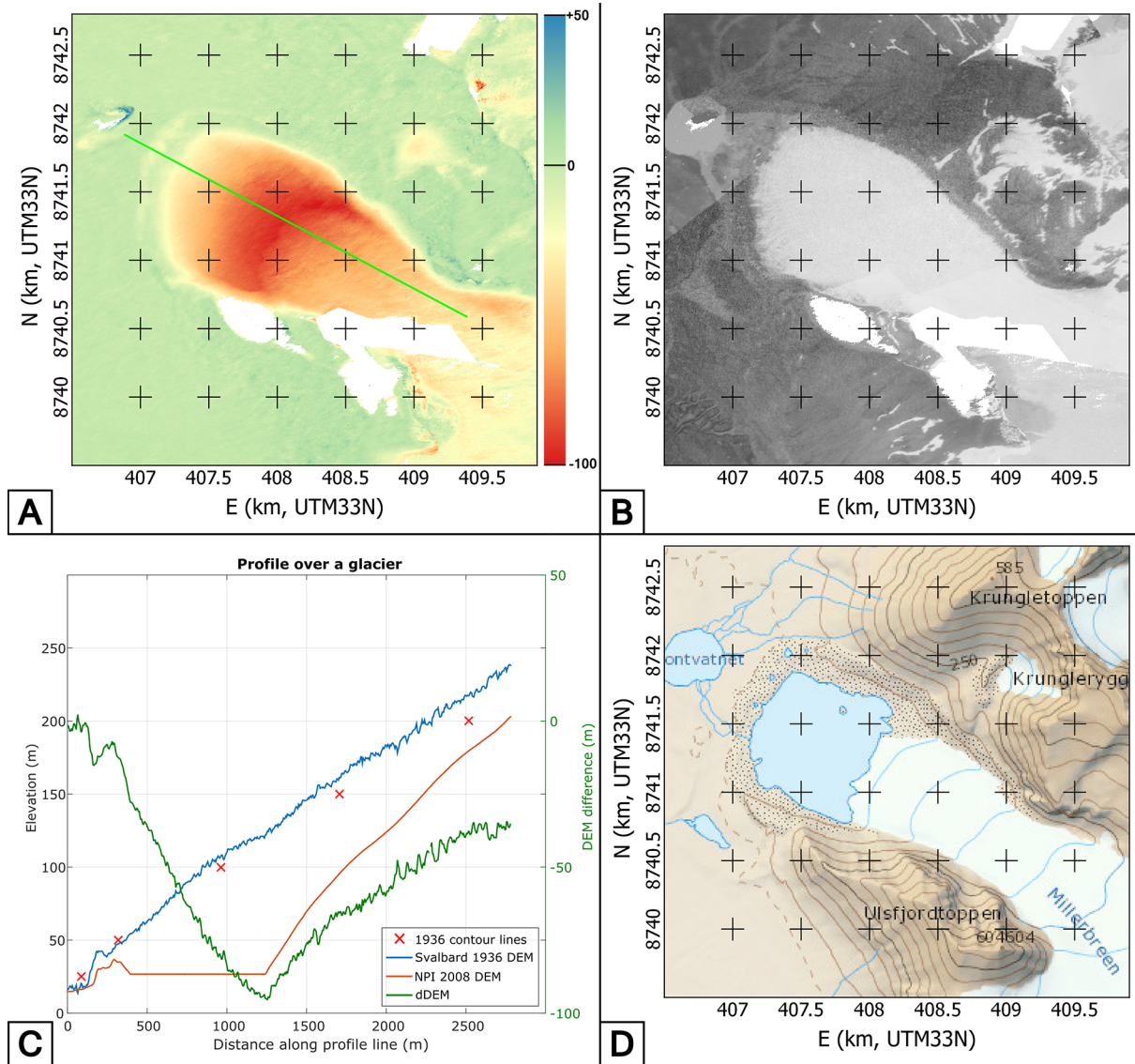
Figure 9. Data over Millerbreeen. A: dDEM between our 1936 and the NPI 2008 DEM and profile line (in green). B: Orthoimage from our 1936 data. C: Profile data on the dDEM and both 1936 and 2008 DEMs, with the data from the original 1936 map contour lines as red crosses. D: Map by NPI made using the 2008 data.

part itself seems to experience a contrasted behavior, with the land terminating part retreating at a significantly lower rate than the marine terminating front. A quite sharp rectangular indent in the glacier front is visible, nearly separating the two parts of the glacier in the 2008 data, and still progressing according the 2010 IDEM data.
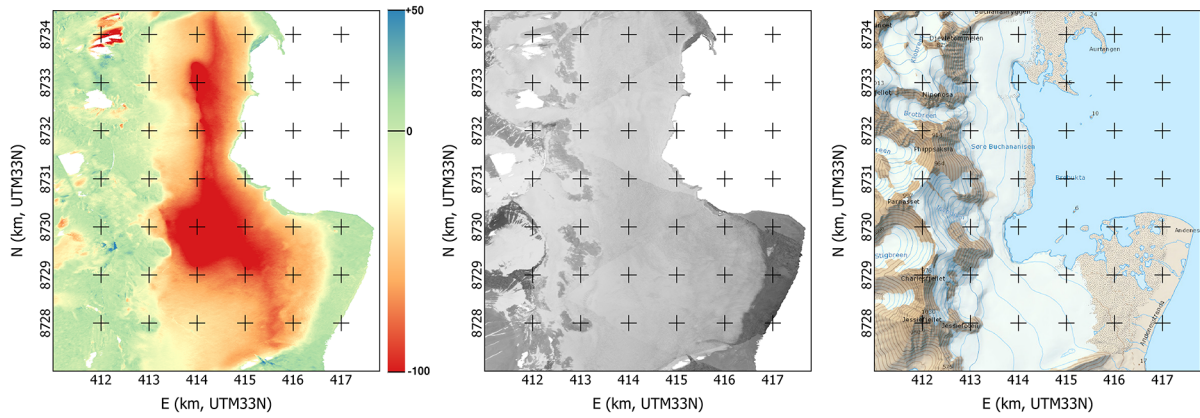
Figure 10. Data over Søre Buchananisen. dDEM between our 1936 and the NPI 2008 DEM. Orthoimage from the 1936 data. Map by NPI made using the 2008 data.

4.2.3 Rock glacier example: unnamed, between the peeks of Monacofjellet and Phippsfjellet

The precision of the data allows for a clear identification of rock glaciers (or ice-cored moraines, or small debris-covered glaciers) and of their changes linked to a degradation process. The example shown here for illustration (Fig. 11) exhibits a maximum elevation loss ($\approx 40\,m$) a third of the way up the landform. The rock glacier front is also flattening (peaking at

5    $\approx 60\,m$ over the valley bottom in 1936, $\approx 50\,m$ in 1990 and $\approx 40\,m$ in 2008). These two observations point to significant ground-ice loss over the 72-year observational period and a topography slowly transforming the whole formation into a talus without abundant ice content.

5 Conclusions

The value of the information contained in historical photogrammetric survey for the study of change in the cryosphere is very

10   obvious, as shown by the increasing amount of scientific literature on the topic. With our processing workflow, we achieve an almost fully automated generation of high quality DEMs even from high oblique photographs. However, such processing still requires some amount of manual work, mostly for GCP identification and for point cloud clean-up. Applied on the imagery taken over Svalbard in 1936, our workflow provides high quality elevation data (STD $2\,m$ for moderate terrain) that allows for the reliable computation of elevation change when compared to more modern data. This may provide an accurate estimate of

15   the retreat and geodetic mass balance of glaciers in the area for the time period since 1936, pushing the beginning of the time series much earlier as previously achievable. The high precision of the data obtained with our workflow also allows for the long term monitoring of processes presenting elevation changes of smaller magnitude such as on rock glaciers.
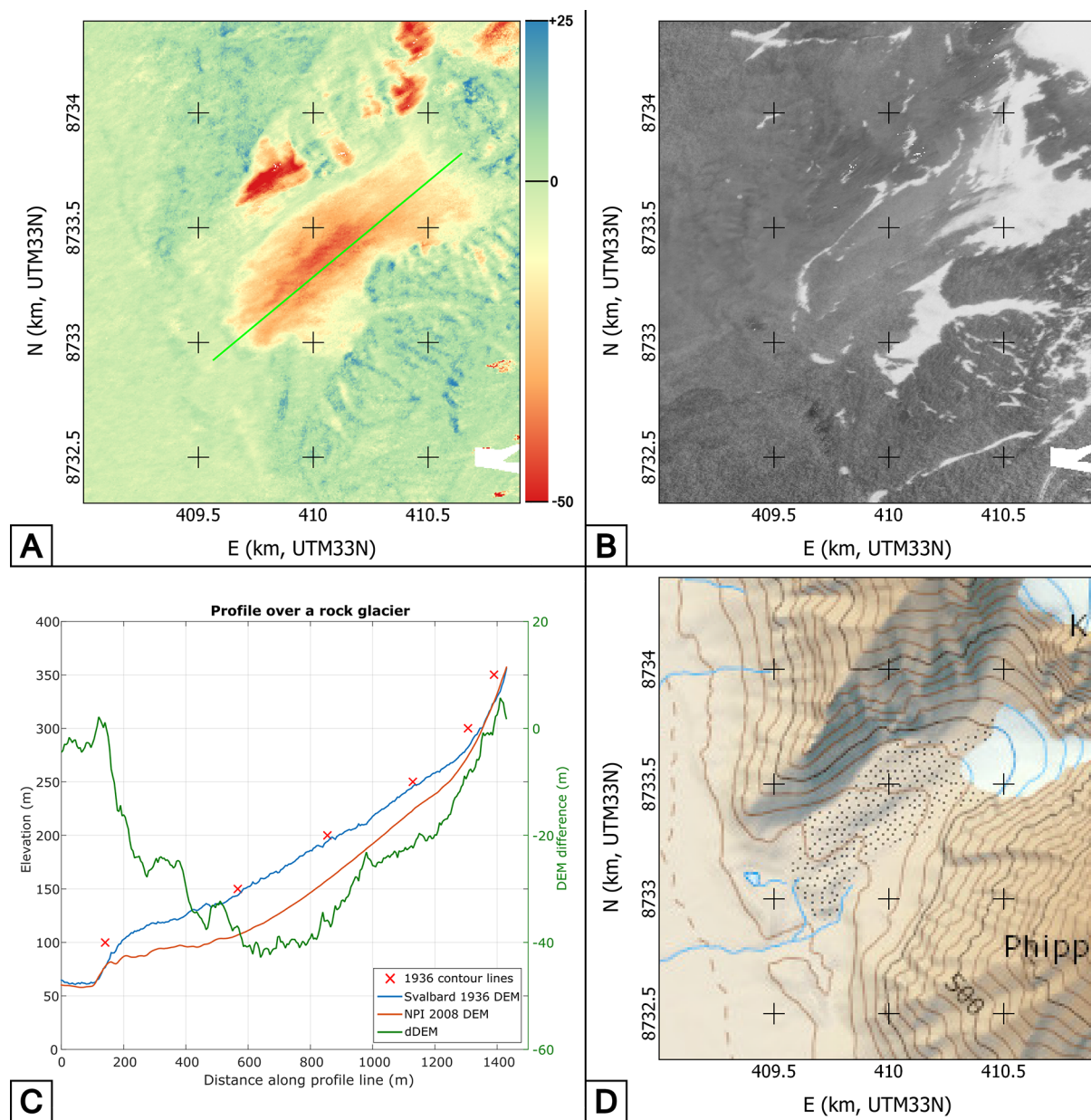
Figure 11. Data over an unnamed rock glacier. A: dDEM between our 1936 and the NPI 2008 DEM and profile line (in green). B: Orthoimage from our 1936 data. C: Profile data on the dDEM and both 1936 and 2008 DEMs, with the data from the original 1936 map contour lines as red crosses. D: Map by NPI made using the 2008 data.

6   Data Availability

Original imagery from NPI. DEM data available upon request.

Author contributions. L. Girod led the research, wrote the paper, processed the data on Prins Karl Forland and supervised the work of N. I. Nielsen and F. Couderette. F. Couderette did an initial assessment of the imagery data and of the potential quality of the products created from it, and designed a first version of the workflow (Couderette, 2016). N. I. Nielsen continued that work and automated most of the process (Nielsen, 2017). C. Nuth and A. Kääb co-supervised the work of N. I. Nielsen and F. Couderette, contributed discussions and edited the
5   paper.

Acknowledgements. The study was funded by the European Research Council under the European Union's Seventh Framework Program (FP/2007-2013)/ERC grant agreement no.320816, the ESA projects Glaciers_cci (4000109873/14/I-NB) and DUE GlobPermafrost (4000116196/15/IN-B). Data scanning and distribution was funded by the Norwegian Polar Institute. Couderette's internship was financed in part through the Erasmus program. We are very grateful to the Norwegian Polar Institute and specifically to Harald F. Aas for providing the raw imagery data
10 for this study as well as the modern validation data. We also acknowledge the help from Marc Pierrot-Deseilligny and the MicMac team at IGN/ENSG for their help in the development of the software.

References

Brown, D. C.: Decentering distortion of lenses, Photometric Engineering, 32, 444–462, 1966.

Brown, D. C.: Close-range camera calibration, Photogramm. Eng, 37, 855–866, 1971.

Child, S., Stearns, L., and Girod, L.: Surface elevation change of Transantarctic Mountain outlet glaciers from 1960 – 2016 using Structure-from-Motion photogrammetry, in: IGS - Polar Ice, Polar Climate, Polar Change - 2017, Boulder, Colorado, USA, 2017.

Couderette, F.: 1936 oblique images : Spreading the time series of Svalbard glacier, Master's thesis, 2016.

Csatho, B. M.: A history of Greenland's ice loss: aerial photographs, remote-sensing observations and geological evidence together provide a reconstruction of mass loss from the Greenland Ice Sheet since 1900–a great resource for climate scientists, Nature, 582, 341–344, 2015.

Etzelmüller, B. and Sollid, J. L.: Long-term mass balance of selected polythermal glaciers on Spitsbergen, Svalbard, Norsk Geografisk Tidsskrift - Norwegian Journal of Geography, 50, 55–66, doi:10.1080/00291959608552352, https://doi.org/10.1080/00291959608552352, 1996.

Furukawa, Y. and Ponce, J.: Accurate, dense, and robust multiview stereopsis, Pattern Analysis and Machine Intelligence, IEEE Transactions on, 32, 1362–1376, doi:https://doi.org/10.1109/TPAMI.2009.161, 2010.

Gomez, C., Hayakawa, Y., and Obanawa, H.: A study of Japanese landscapes using structure from motion derived DSMs and DEMs based on historical aerial photographs: New opportunities for vegetation monitoring and diachronic geomorphology, Geomorphology, 242, 11–20, 2015.

Kääb, A.: Monitoring high-mountain terrain deformation from repeated air-and spaceborne optical data: examples using digital aerial imagery and ASTER data, ISPRS Journal of Photogrammetry and remote sensing, 57, 39–52, 2002.

Lowe, D. G.: Distinctive Image Features from Scale-Invariant Keypoints, Int. J. Comput. Vision, 60, 91–110, doi:10.1023/B:VISI.0000029664.99615.94, http://dx.doi.org/10.1023/B:VISI.0000029664.99615.94, 2004.

Luncke, B.: Luftkartlegningen på Svalbard 1936, 1936.

Mertes, J. R., Gulley, J. D., Benn, D. I., Thompson, S. S., and Nicholson, L. I.: Using structure-from-motion to create glacier DEMs and orthoimagery from historical terrestrial and oblique aerial imagery, Earth Surface Processes and Landforms, pp. n/a–n/a, doi:10.1002/esp.4188, http://dx.doi.org/10.1002/esp.4188, eSP-16-0346.R2, 2017.

Midgley, N. G. and Tonkin, T. N.: Reconstruction of former glacier surface topography from archive oblique aerial images, Geomorphology, 282, 18–26, 2017.

Mölg, N. and Bolch, T.: Structure-from-Motion Using Historical Aerial Images to Analyse Changes in Glacier Surface Elevation, Remote Sensing, 9, doi:10.3390/rs9101021, http://www.mdpi.com/2072-4292/9/10/1021, 2017.

Nielsen, N. I.: Recovering Data with Digital Photogrammetry and Image Analysis Using Open Source Software - 1936 Aerial Photographs of Svalbard, Master's thesis, 2017.

Nuth, C., Kohler, J., Aas, H., Brandt, O., and Hagen, J.: Glacier geometry and elevation changes on Svalbard (1936–90): a baseline dataset, Annals of Glaciology, 46, 106–116, 2007.

Vargo, L. J., Anderson, B. M., Horgan, H. J., Mackintosh, A. N., Lorrey, A. M., and Thornton, M.: Using structure from motion photogrammetry to measure past glacier changes from historic aerial photographs, Journal of Glaciology, 63, 1105–1118, 2017.